

Band-Gap Reduction in $(\text{BiCrO}_3)_m/(\text{BiFeO}_3)_n$ Superlattices: Designing Low-Band-Gap Ferroelectrics

S. Zhang,¹ H.Y. Xiao,^{1,*} S.M. Peng,² G.X. Yang,² Z.J. Liu,³ X.T. Zu,¹ S. Li,⁴ D.J. Singh,⁵ L.W. Martin,^{6,7} and L. Qiao^{1,4,†}

¹*School of Physics, University of Electronic Science and Technology of China, Chengdu 610054, China*

²*Institute of Nuclear Physics and Chemistry, Chinese Academy of Engineering Physics, Mianyang 621900, China*

³*Department of Physics, Physics, Lanzhou City University, Lanzhou 730070, China*

⁴*School of Materials, University of New South Wales, Sydney, Australia*

⁵*Department of Physics and Astronomy, University of Missouri, Columbia, Missouri 65211-7010, USA*

⁶*Department of Materials Science and Engineering, University of California, Berkeley, Berkeley, California 94720, USA*

⁷*Materials Sciences Division, Lawrence Berkeley National Laboratory, Berkeley, California 94720, USA*

(Received 24 March 2018; revised manuscript received 24 July 2018; published 2 October 2018)

Ferroelectric BiFeO₃ is promising for photovoltaic applications, especially in regard to the exploitation of ferroelectric photovoltaic effects for charge separation. However, its large band gap limits efficient sunlight absorption. Here, we demonstrate a new strategy to effectively tune the band gap of tetragonal BiFeO₃ via superlattice structuring with the ferroelectric BiCrO₃. The $(\text{BiCrO}_3)_m/(\text{BiFeO}_3)_n$ superlattices are found to exhibit conventional ferroelectric properties, but low fundamental band gaps, smaller than either of the parent materials. First-principles calculations reveal that the unexpected band-gap reduction is induced by charge reconstruction due to lattice strain, octahedral distortion, and polarization discontinuity at the BiCrO₃-BiFeO₃ interfaces. Ultimately, these results provide a new strategy, in the form of superlattice structuring, which could open the door to the creation of efficient ferroelectric photovoltaics.

DOI: 10.1103/PhysRevApplied.10.044004

I. INTRODUCTION

In the past several decades, researchers have been striving to open different corridors for the production of renewable energy. In this regard, photovoltaics (PVs) have been demonstrated to be a promising renewable energy technology to harvest solar energy [1–3], one of the most abundant energy sources available on Earth [4]. Generally, the performance of PV materials is quantified by the power conversion efficiency (PCE), which can be related to the photovoltage and photocurrent. Recently, building from the initial interest in single-crystal and ceramic materials over four decades ago [5], a rejuvenation of interest in the so-called anomalous photovoltaic effect in noncentrosymmetric thin-film ferroelectrics has driven an urgent search for new materials in this space. Contrary to traditional semiconductor-based PVs, the photovoltage of ferroelectrics is not limited by their band gap, but can be a few orders of magnitude larger than the optical band gap of the material itself [5,6]. In some cases, the photovoltage has been found to be $>10^4$ V [2,6]. Generally, the photovoltage is proportional to the magnitude of the electric polarization

[6–9]; however, the PCE of ferroelectric materials is normally limited by their small photocurrent density, typically on the order of nA/cm², which mainly originates from the large intrinsic band gap of these materials (typically 3–4 eV) [2,10]. It is, therefore, of significant importance to lower the band gap of ferroelectric materials without affecting the ferroelectric polarization in an attempt to improve the PCE in PV applications. This is also of great importance for fully characterizing ferroelectric photovoltaic effects, including understanding the performance limits of these devices. While ferroelectric semiconductors do exist [11], for reasons yet to be understood, the largest effects are observed in oxides, and therefore, finding better oxide materials is a key challenge in the field.

A focus has been in BiFeO₃ due to its intrinsic, relatively low band gap (2.67–3.1 eV) [12] and high polarization (90–158 $\mu\text{C}/\text{cm}^2$) [13–15]. Importantly, BiFeO₃ has been widely investigated for PV applications and so far shows better PCE efficiency than most other ferroelectric materials [2,16–20], making it a highly desirable ingredient in fabricating new ferroelectric photovoltaics. Despite these successes, however, BiFeO₃ can only absorb UV light, which constitutes only approximately 20% of the entire solar spectrum, leaving most of the solar energy incident on Earth unexploited [21]. In epitaxial

*hyxiao@uestc.edu.cn

†liang.qiao@uestc.edu.cn

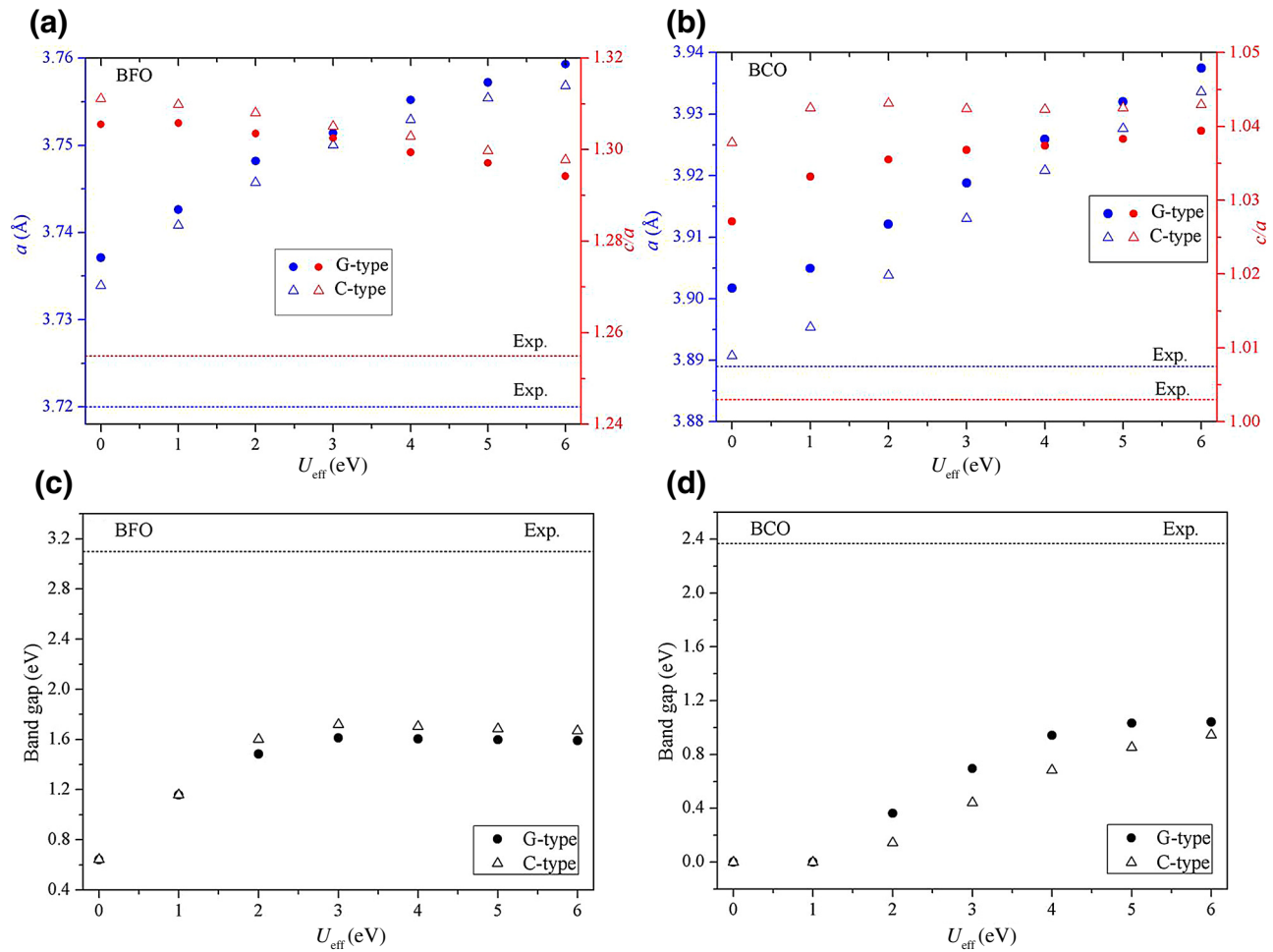


FIG. 1. Variation of lattice parameter a (lattice constants a in blue and c/a ratio in red) for (a) G- and C-type BFO and (b) G- and C-type BCO as a function of U_{eff} value, and variation of band gap for (c) G- and C-type BFO and (d) G- and C-type BCO as a function of U_{eff} value. The dashed lines are the experimental results.

BiFeO_3 thin films, there are several possible phases, including structures derived from monoclinic, triclinic, orthorhombic, and tetragonal parent structures. Of particular note is the tetragonal-like phase, which is actually a slightly monoclinically-distorted tetragonal structure, and has a large c/a lattice parameter ratio of approximately 1.26 and a giant spontaneous polarization approaching approximately $150 \mu\text{C}/\text{cm}^2$. With this in mind, it is meaningful to reduce the band gap of tetragonal-like BiFeO_3 , while maintaining the large spontaneous polarization, to enhance the PCE. On the other hand, BiCrO_3 is another ferroelectric material, also with an active lone pair on the bismuth cation [22], which is often used to tune the band gap and photocurrent of BiFeO_3 [23–26], e.g., through alloying. We have recently studied alloyed BiCrO_3 - BiFeO_3 films and found that chromium substitution can help to reduce the band gap by approximately 0.8 eV for solid solution films and improves charge transport [27]. The BiCrO_3 / BiFeO_3 bilayer films, synthesized using a sol-gel technique, were

found to exhibit a band gap of approximately 2.25 eV (smaller than the value of 2.64 eV of BiFeO_3) and a short circuit photocurrent density of $0.08 \text{ mA}/\text{cm}^2$ (higher than the value of $0.007 \text{ mA}/\text{cm}^2$ for a single-layer BiFeO_3 film) [28]. Multiferroic BiFeO_3 / BiCrO_3 heterostructures have also been studied experimentally [10], and it was reported that the photocurrent density and photovoltage can be tuned by the thickness and the number of BiFeO_3 / BiCrO_3 bilayers and that the highest photocurrent density value (approximately $0.013 \text{ mA}/\text{cm}^2$) was recorded in 60-nm-thick heterostructures (including two BiFeO_3 / BiCrO_3 bilayers with each layer of a thickness of 15 nm).

More recently, significant band-gap reduction has been realized in double-perovskite $\text{Bi}_2\text{CrFeO}_6$, in which B -sitecation ordering controlled by film synthesis results in a remarkable PCE of over 8.1% under air mass (AM) 1.5 G irradiation [21]; a new record for inorganic perovskites in conventional solar-cell applications. The mechanism

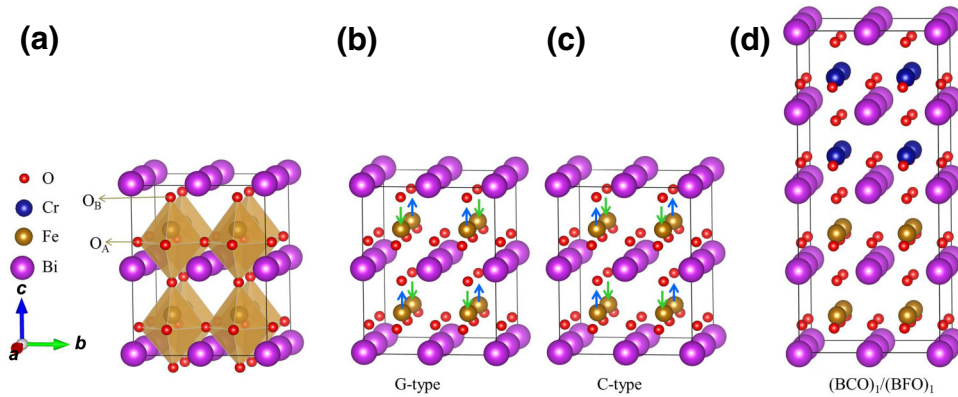


FIG. 2. Schematic view of (a) $2 \times 2 \times 2$ supercell for BFO; (b) BFO with a G-type AFM state; (c) BFO with a C-type AFM state; and (d) optimized $(\text{BCO})_1/(\text{BFO})_1$ superlattice.

of enhanced visible-light absorption and its correlation with cation ordering in the double-perovskite $\text{Bi}_2\text{CrFeO}_6$, however, is not clear. It is well known that for perovskites, achieving *B*-site-cation ordering is very difficult (and it is particularly sensitive to oxygen partial pressure and growth temperature) as the thermodynamic window allowing for the realization of such ordered states is extremely narrow. This has been shown true in a number of systems, including La_2VMnO_6 [29], $\text{La}_2\text{CrFeO}_6$ [30], $\text{La}_2\text{NiMnO}_6$ [31], etc. On the other hand, superlattice ordering is also a powerful method to engineer ordered double-perovskite structures. For example, long-range ferromagnetism has been reported in $\text{LaCrO}_3/\text{LaFeO}_3$ superlattices, which is unexpected, given that both LaCrO_3 and LaFeO_3 are antiferromagnetic [32–34]. Therefore, by creating an atomically-ordered state via superlattice structuring of the aforementioned BiFeO_3 and BiCrO_3 , one might expect to yield interesting electronic structure and material properties, distinct from alloys. There are limited studies on $\text{BiCrO}_3/\text{BiFeO}_3$ superlattices, and those which do exist are focused mainly on traditional ferroelectric behavior. For example, using a scanning nonlinear dielectric microscope, researchers found that the polarization in

such superlattices is reversible and thus suggested that the superlattices are ferroelectric at room temperature [35]. The ground state properties of $\text{BiFeO}_3/\text{BiCrO}_3$ superlattices, such as the electronic structure, intrinsic band gap, and ferroelectric polarization, are, however, not well developed.

Here, we report a density functional theory (DFT) investigation of the lattice geometrical and electronic properties of $(\text{BiCrO}_3)_m/(\text{BiFeO}_3)_n$ superlattices. Systematic study shows that the band gap of the superlattices is widely tunable, and can take values well below those of either component by itself, while still maintaining the ferroelectric polarization. Unexpectedly, the optimized band gap of approximately 1.6 eV for the $\text{BiCrO}_3/\text{BiFeO}_3$ superlattice is not only smaller than both the single-layer BiFeO_3 and BiCrO_3 , but is also smaller than the equivalent $\text{Bi}(\text{Fe}, \text{Cr})\text{O}_3$ alloy [27]. This surprising result is the consequence of charge reconstruction due to lattice strain, octahedral distortion, and polarization discontinuity at the superlattice interfaces. We also show that the ferroelectric and magnetic properties of the superlattice are not strongly affected. These results demonstrate that superlattice structuring can be an effective strategy for

TABLE I. The structural parameters and band gap (E_g) of BFO and BCO with G-type and C-type AFM spin states. $\angle O_A\text{-}M\text{-}O_B$: bond angle ($M = \text{Fe}$ or Cr); MM: magnetic moment of Fe and Cr.

Compounds		a (Å)	c (Å)	c/a	$\angle O_A\text{-}M\text{-}O_B$ (°)	E_g (eV)	MM (μ_B)
BFO	G-type AFM	3.755	4.879	1.300	110.7	1.62	4.136
	C-type AFM	3.753	4.890	1.303	110.9	1.71	4.130
	Exp. ^{a,b,c}	3.72	4.67	1.255		3.1	4.34
	Other cal. ^d					1.90	4.18
BCO	G-type AFM	3.926	4.073	1.037	96.6	0.94	2.944
	C-type AFM	3.921	4.087	1.042	96.7	0.69	2.923
	Exp. ^{e,f}	3.889	3.902	1.003		2.37	

^aRef. [42].

^bRef. [46].

^cRef. [45].

^dRef. [44].

^eRef. [28].

^fRef. [52].

the design of low band gap oxide semiconductors with fundamental band gaps much smaller than that of either parent material, thus opening new perspectives for ferroelectric PVs.

II. COMPUTATIONAL DETAILS

All of the spin-polarized calculations are carried out based on the DFT, using the Vienna ab-initio Simulation Package (VASP) code [36,37]. For the exchange and correlation energy, the Perdew-Burke-Ernzerhof (PBE) functional [38] under the generalized gradient approximation (GGA) is employed. The on-site Coulomb interaction presented in $3d$ states of transition-metal ions are corrected by the DFT + U (where U is the Hubbard energy) method [39]. The dependence of the lattice parameters and band gap for BiFeO_3 on the effective U value are presented [Figs. 1(a) and 1(c)]. It is shown that as the U_{eff} value increases, the lattice parameter a and c/a deviate from and approach the experimental values, respectively. On the other hand, the band gap increases until $U_{\text{eff}} = 3$ eV and any further increase has slight influence on the band gap. For BiCrO_3 , a similar trend is observed. Consequently, the $U_{\text{eff}} = 4$ eV [27,40] is employed for both Fe $3d$ and Cr $3d$ states in this work. A cutoff energy of 500 eV for plane-wave basis set and a $4 \times 4 \times 4$ Monkhorst-Pack k-mesh for Brillouin-zone integrations are used for structural relaxation. The convergence criteria for total energies and forces are 10^{-4} eV and 10^{-4} eV/Å, respectively. During the structural optimization, a full relaxation is employed. The spontaneous polarization is evaluated by simply summing the product of atomic displacements and corresponding Born effective charges (BECs) [41], which are calculated using density functional perturbation theory with a $2 \times 2 \times 2$ Monkhorst-Pack k-mesh. For bulk BiFeO_3 (BFO), and BiCrO_3 (BCO), all computations are based on a $2 \times 2 \times 2$ supercell containing 40 atoms. For the $(\text{BiCrO}_3)_m/(\text{BiFeO}_3)_n$ [$(\text{BCO})_m/(\text{BFO})_n$] superlattices, which consist of m unit cells of BCO alternating with n unit cells of BFO, different alternating periodic cells, i.e., $(\text{BCO})_m/(\text{BFO})_1$ and $(\text{BCO})_1/(\text{BFO})_n$ ($m, n = 1, 2, 3, 4, 5$), are considered.

III. RESULTS AND DISCUSSION

A. Ground state properties of bulk BFO and BCO

The tetragonal-like phase of BFO with a space group of $P4mm$ has a large c/a lattice parameter ratio (1.255–1.27) [12,42], where O_A and O_B , respectively, belong to the FeO and BiO layers [Fig. 2(a)]. Clearly, one Fe^{3+} is coordinated by six O^{2-} ions and an octahedron is formed. In the literature, it has been reported that the tetragonal-like BFO has G- and C-type antiferromagnetic spin states [40,43]. Schematic views of the spin configurations of BFO are

illustrated [Figs. 2(b) and 2(c)]; in this work, both G- and C-type ordering are considered for bulk BFO and BCO.

For bulk BFO, the obtained lattice parameters of $a = 3.755$ Å and $c/a = 1.300$ for G-type ordering are close to the calculated values of 3.753 Å and 1.303, respectively, for C-type ordering; both are in good agreement with the experimental values of 3.72 Å and 1.255 [42], respectively. The calculated magnetic moment of Fe is $4.136 \mu_B/\text{atom}$ for G-type ordering, agreeing well with the prior theoretical value of $4.18 \mu_B/\text{atom}$ [44] and the experimental value of $4.34 \mu_B/\text{atom}$ [45], and it is comparable to the result of $4.130 \mu_B/\text{atom}$ for C-type ordering. Both G- and C-type ordered BFO exhibit direct band gaps and the values of the band gaps are 1.62 and 1.71 eV, respectively; which are smaller than the experimental data of 3.1 eV

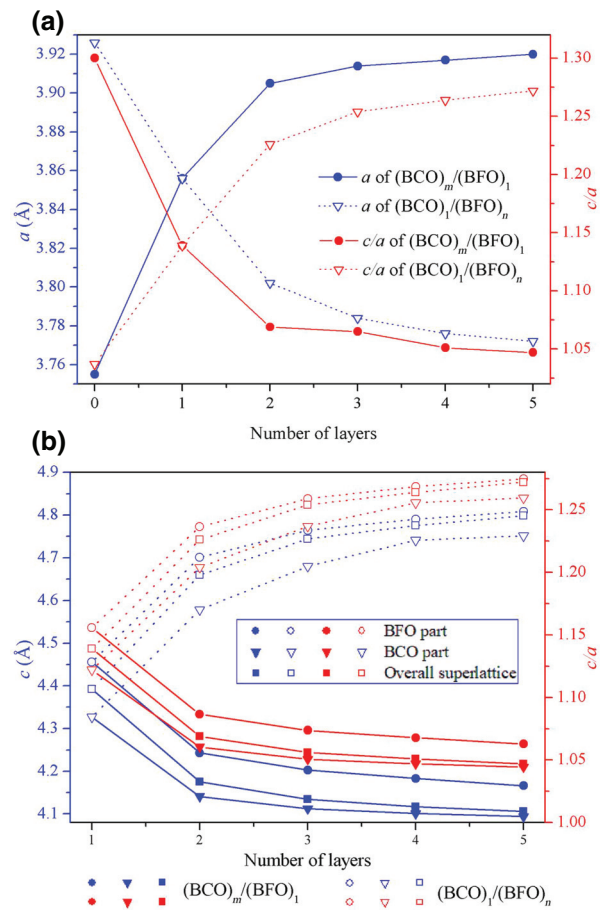


FIG. 3. (a) Variation of lattice constants a (blue) and c/a (red) for $(\text{BCO})_m/(\text{BFO})_1$ and $(\text{BCO})_1/(\text{BFO})_n$ ($m, n = 0, 1, 2, 3, 4, 5$) as a function of the number of layers; (b) variation of out-of-plane lattice constants c (blue) and c/a (red) for $(\text{BCO})_m/(\text{BFO})_1$ (solid) and $(\text{BCO})_1/(\text{BFO})_n$ (hollow) ($m, n = 0, 1, 2, 3, 4, 5$) as a function of the number of layers. The circle sign is the average of the BFO part in the superlattice, the triangle down sign is the average of the BCO part in the superlattice, and the square sign is the average of the overall superlattices.

TABLE II. The calculated lattice parameters (the values of c and c/a are the average values of overall superlattices), average interlayer distance Δd , and bond angles of BFO, BCO, and $(\text{BCO})_m/(\text{BFO})_n$ superlattices.

Compounds	a (Å)	c (Å)	c/a	Δd_{BFO} (Å)	Δd_{BCO} (Å)	$\angle O_A\text{-Cr}-O_B$ (°)	$\angle O_A\text{-Fe}-O_B$ (°)
BFO	3.755	4.879	1.300	4.879			110.7
BCO	3.926	4.073	1.037		4.073	96.6	
$(\text{BCO})_1/(\text{BFO})_1$	3.856	4.392	1.139	4.456	4.327	100.7	105.0
$(\text{BCO})_2/(\text{BFO})_1$	3.905	4.175	1.069	4.243	4.141	97.91	101.1
$(\text{BCO})_3/(\text{BFO})_1$	3.914	4.134	1.056	4.203	4.112	97.4	100.2
$(\text{BCO})_4/(\text{BFO})_1$	3.917	4.117	1.051	4.183	4.101	97.2	99.8
$(\text{BCO})_5/(\text{BFO})_1$	3.920	4.106	1.047	4.166	4.094	97.0	99.5
$(\text{BCO})_1/(\text{BFO})_2$	3.802	4.660	1.226	4.701	4.578	104.8	108.3
$(\text{BCO})_1/(\text{BFO})_3$	3.784	4.744	1.254	4.764	4.680	106.1	109.2
$(\text{BCO})_1/(\text{BFO})_4$	3.776	4.775	1.264	4.790	4.741	106.6	109.5
$(\text{BCO})_1/(\text{BFO})_5$	3.772	4.798	1.272	4.808	4.751	107.1	109.8

[12,46,47]. This is a generic problem in DFT, which persists in the PBE + U calculations, with $U=4$ eV. Higher values of U have slight effects on the band gap, and so we use $U=4$ eV, and correct the band gap using a scissors operation [48,49] based on the known experimental gap of BFO and BCO (see part C of Sec. III). Our calculations show that the geometric structure, band structure, and Fe magnetic moment of G- and C-type ordered tetragonal BFO are similar to each other, which is consistent with previous theoretical studies [40]. We also find that the total energy difference between G- and C-type ordered BFO is only 0.068 eV, indicating that the stability of these two orderings are comparable.

For bulk G- and C-type ordered BCO, the obtained magnetic moment of Cr and the lattice parameters are, as for the case of BFO, similar to each other (Table I). For G-type ordered BCO, the calculated lattice parameters are $a=3.926$ Å and $c=4.073$ Å, which are comparable to the experimental results of $a=3.888$ Å and $c=3.902$ Å [50]. On the other hand, the band gap of 0.94 eV for G-type ordering is higher than the value of 0.69 eV for C-type ordering, and both values are smaller than the experimental value of 2.37 eV [28]. The calculated band gaps of BCO (0.94 eV for G-type and 0.69 eV for C-type) are smaller than those of BFO (1.62 eV for G-type and 1.71 eV for C-type), consistent with the experimental results. [12,28]. In addition, the total energy of the G-type ordering is 0.156 eV smaller than C-type ordering, i.e., the G-type ordering BCO is energetically more preferable. Hence, in the subsequent calculations, we only consider the BFO and BCO with G-type ordering.

B. Geometric structures of the superlattices

Figure 2(d) illustrates the geometric structure for the optimized $(\text{BCO})_1/(\text{BFO})_1$ superlattice. The optimized structural parameters of $(\text{BCO})_m/(\text{BFO})_1$ and $(\text{BCO})_1/(\text{BFO})_n$ superlattices are also presented (Table II), including data for bulk BFO and BCO. The calculated

lattice constant a and average c/a ratio as a function of m and n are also plotted [Fig. 3(a)]. It is found that the in-plane lattice constant a of $(\text{BCO})_m/(\text{BFO})_1$ increases with increasing BCO layers, and the in-plane lattice constant of $(\text{BCO})_1/(\text{BFO})_n$ decreases with increasing BFO layers, owing to the strain effect caused by the lattice mismatch between BFO and BCO. However, as can be seen [Fig. 3(b)], the average out-of-plane lattice constant c of the superlattices decreases with increasing BCO layers and increases with increasing BFO layers. For displacive ferroelectric materials, the c/a ratio reflects the tetragonal distortion, which is a consequence of the spontaneous polarization. Therefore, the observed increase of the c/a ratio indicates an increase of relative displacement between cations and anions, resulting in enhanced polarization [51,52]. The c/a ratio decreases with increasing BCO layers and increases with increasing BFO layers [Fig. 3(b)], indicating that the polarization of the $(\text{BCO})_1/(\text{BFO})_n$ superlattices is larger than that of the $(\text{BCO})_m/(\text{BFO})_1$ superlattices. This is directly seen in the polarization we discuss in the next section. It is thus expected that the electrical and optical properties of the $(\text{BCO})_m/(\text{BFO})_n$ superlattices can be adjusted by tuning the stacking period, which will alter the ground-state structure of the superlattices due to strain effects [52].

TABLE III. The calculated formation energies for $(\text{BCO})_m/(\text{BFO})_n$ superlattices.

Superlattices	Formation energy (eV)
$(\text{BCO})_1/(\text{BFO})_1$	1.94
$(\text{BCO})_2/(\text{BFO})_1$	2.36
$(\text{BCO})_3/(\text{BFO})_1$	2.46
$(\text{BCO})_4/(\text{BFO})_1$	2.50
$(\text{BCO})_5/(\text{BFO})_1$	2.51
$(\text{BCO})_1/(\text{BFO})_2$	2.50
$(\text{BCO})_1/(\text{BFO})_3$	2.70
$(\text{BCO})_1/(\text{BFO})_4$	2.81
$(\text{BCO})_1/(\text{BFO})_5$	2.86

The average interlayer distance Δd (the thickness of one monolayer, which is equivalent to the local out-of-plane lattice constant) and the bond angles $\angle O_A\text{-Cr}\text{-}O_B$ and $\angle O_A\text{-Fe}\text{-}O_B$ in BFO, BCO, and the $(\text{BCO})_m/(\text{BFO})_n$ superlattices are also summarized (Table II). We find that all the values of Δd_{BFO} for superlattices are smaller than the value of 4.879 Å for bulk BFO and the values of Δd_{BCO} are larger than the value of 4.073 Å for bulk BCO, indicating that the BFO in the $(\text{BCO})_1/(\text{BFO})_n$ superlattices is compressed, while the BCO in the $(\text{BCO})_m/(\text{BFO})_1$ superlattices is stretched along the [001] direction in comparison to their bulk values. This is a result of the interface stress caused by the large lattice mismatch (4.3%) between the BFO and BCO, since the lattice constant of BFO (3.755 Å) is much smaller than that of BCO (3.926 Å). For the $(\text{BCO})_m/(\text{BFO})_1$ superlattices, as the number of BCO layers increases from 1 to 5, Δd_{BFO} decreases from 4.456 to 4.166 Å, and Δd_{BCO} decreases from 4.327 to 4.094 Å. Obviously, for the thicker BCO layers, the interlayer spacing of BFO is far from that in the bulk state and the interlayer distance between BCO layers becomes close to that in the bulk. Correspondingly, the $\angle O_A\text{-Fe}\text{-}O_B$ angle deviates much more from the 110.7° in the bulk state and the $\angle O_A\text{-Cr}\text{-}O_B$ angle approaches the 96.6° in the bulk state. These results suggest that the thicker BCO layers lead to significant compression of the BFO and large relaxation of the BCO layers along the [001] direction. As for the $(\text{BCO})_1/(\text{BFO})_n$ superlattices, when the BFO layer is increased in thickness from 1 to 5 unit cells, the BFO layer is compressed and the BCO layer is expanded considerably, resulting in Δd_{BFO} and $\angle O_A\text{-Fe}\text{-}O_B$ approaching the bulk values for BFO and Δd_{BCO} and $\angle O_A\text{-Cr}\text{-}O_B$ deviating significantly from the bulk values for BCO. Comparing the bond angles $\angle O_A\text{-Cr}\text{-}O_B$ and $\angle O_A\text{-Fe}\text{-}O_B$ in both the $(\text{BCO})_1/(\text{BFO})_n$ and $(\text{BCO})_m/(\text{BFO})_1$ superlattices, we find that both angles in the $(\text{BCO})_1/(\text{BFO})_n$ superlattices are larger than those in the $(\text{BCO})_m/(\text{BFO})_1$ superlattices, indicating that the distortion of the octahedra in the tetragonal lattice of the $(\text{BCO})_1/(\text{BFO})_n$ superlattices is more significant, which results in a larger c/a ratio and polarization [51]. This is in good agreement with the discussions in the above section. It is obvious that the induced structural deformation and octahedral distortion in the $(\text{BCO})_1/(\text{BFO})_n$ and $(\text{BCO})_m/(\text{BFO})_1$ superlattices are different, indicating that they may exhibit different electronic structures and polarizations.

The formation of these superlattices can be quantitatively estimated by their respective formation energy, which reflects the total energy cost during the superlattice structuring of the two parent compounds, BFO and BCO. The formation energies of $(\text{BCO})_m/(\text{BFO})_n$ superlattices as compared to bulk BFO and BCO are calculated and the results are summarized (Table III). The formation energy is defined as $E = E_{(\text{BCO})_m/(\text{BFO})_n} - nE_{\text{bulkBFO}} - mE_{\text{bulkBCO}}$. Here, $E_{(\text{BCO})_m/(\text{BFO})_n}$, E_{bulkBFO} , and E_{bulkBCO} are

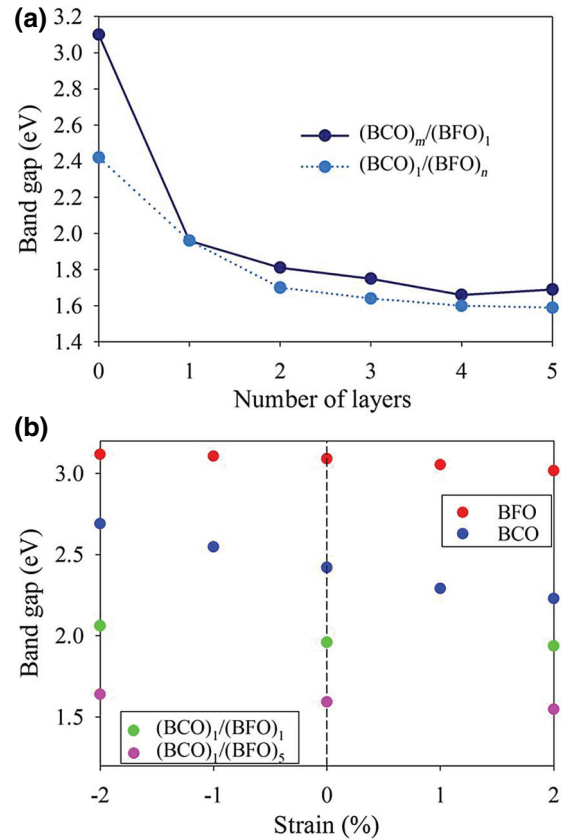


FIG. 4. (a) Variation of band gaps for $(\text{BCO})_m/(\text{BFO})_1$ and $(\text{BCO})_1/(\text{BFO})_n$ ($m, n = 1, 2, 3, 4, 5$) as a function of number of layers; (b) variation of band gap for bulk BFO and BCO as a function of strain. The negative values indicate compressive strain and the positive values indicate tensile strain.

the total energies of $(\text{BCO})_m/(\text{BFO})_n$ superlattices, bulk BFO, and bulk BCO, respectively. As shown in Table III, the $(\text{BCO})_1/(\text{BFO})_1$ superlattice has the lowest formation energy of 1.94 eV among the considered superlattices, and the formation energies of $(\text{BCO})_m/(\text{BFO})_1$ and $(\text{BCO})_1/(\text{BFO})_n$ superlattices increase with the increasing layer numbers of BCO and BFO, respectively. It is also noted that the formation energy of $(\text{BCO})_m/(\text{BFO})_1$ is relatively smaller than that of $(\text{BCO})_1/(\text{BFO})_n$ ($m = n = 2, 3, 4, 5$). These results suggest that as the layer number of BFO or BCO is increased, the $(\text{BCO})_m/(\text{BFO})_1$ and $(\text{BCO})_1/(\text{BFO})_n$ superlattices become more difficult to form, and the $(\text{BCO})_1/(\text{BFO})_n$ superlattices are relatively more difficult to form than the $(\text{BCO})_m/(\text{BFO})_1$ superlattices.

In order to investigate whether the superlattice structures are mechanically stable, we select the $(\text{BCO})_1/(\text{BFO})_1$ superlattice as a model system and calculate its elastic constants. The obtained elastic constants are C_{11} of 260.1 GPa, C_{33} of 64.4 GPa, C_{44} of 79.1 GPa, C_{66} of 59.4 GPa, C_{12} of 75.3 GPa, and C_{13} of 78.3 GPa, which

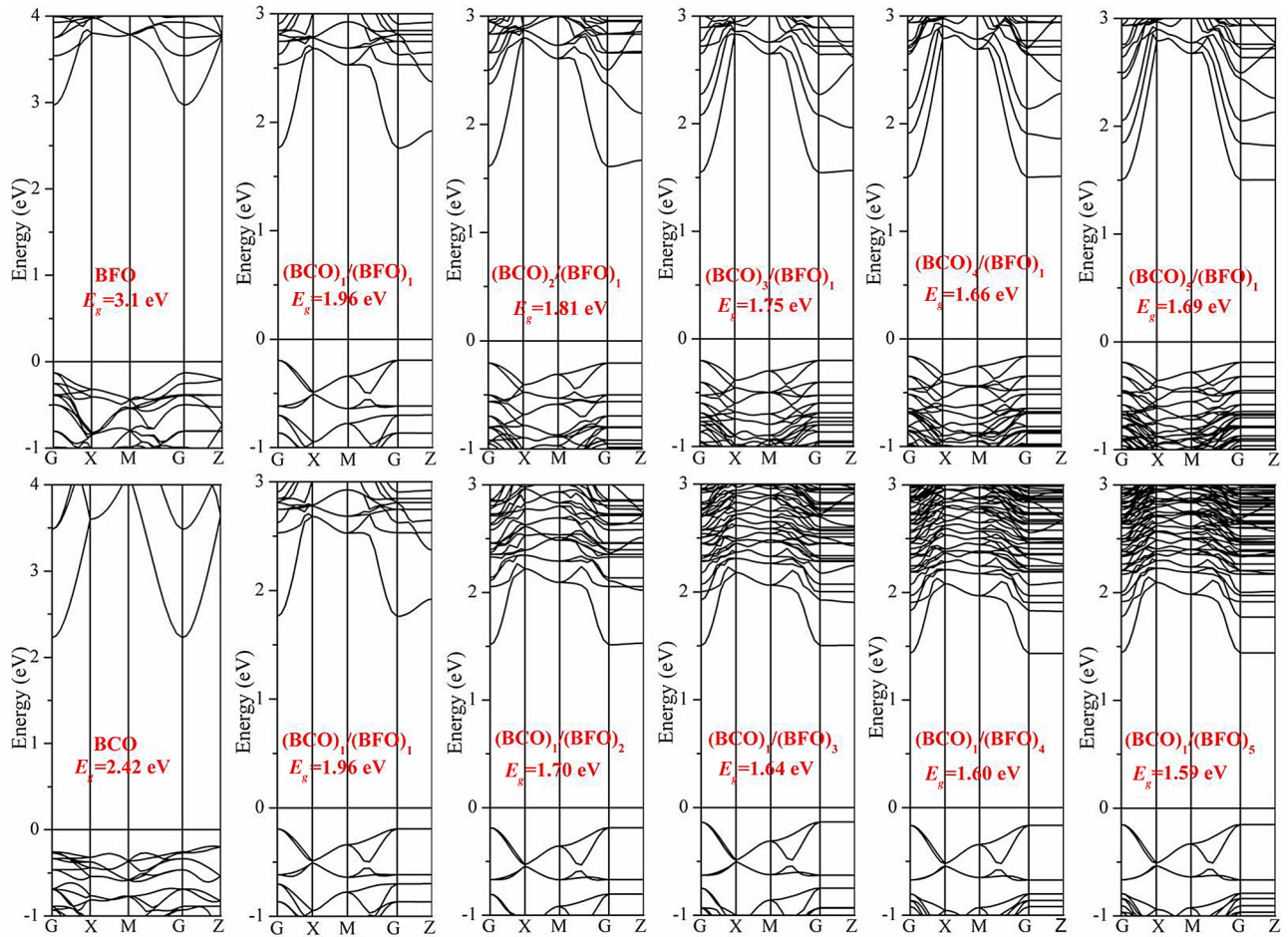


FIG. 5. Band structures of bulk BFO, BCO, $(\text{BCO})_m/(\text{BFO})_1$, and $(\text{BCO})_1/(\text{BFO})_n$ ($m, n = 1, 2, 3, 4, 5$) superlattices. The Fermi level is located at 0 eV.

satisfy the Born stability criteria, i.e., $C_{11} > 0$, $C_{33} > 0$, $C_{44} > 0$, $C_{66} > 0$, $(C_{11}-C_{12}) > 0$, $(C_{11}+C_{33}-2C_{13}) > 0$, $[2(C_{11}+C_{12})+C_{33}+4C_{13}] > 0$, indicating that the $(\text{BCO})_1/(\text{BFO})_1$ superlattice is mechanically stable. The lattice mismatch between bulk BFO and BCO is about 4.3%. Experimentally, the $\text{LaAlO}_3/\text{BaTiO}_3$, $\text{PbTiO}_3/\text{PbZrO}_3$, and $\text{BaZrO}_3/\text{SrTiO}_3$ superlattices, for which the lattice mismatches are 5.3%, 5.3%, and 6.9%, respectively, have been synthesized successfully by Zuo *et al.* [53], Choi *et al.* [54], and Christen *et al.* [55], respectively. Hence, the BFO/BCO superlattice, with a lattice mismatch of approximately 4.3%, is possible to synthesize with an appropriate substrate. Recently, the supertetragonal phase of BFO has been successfully synthesized by various groups via epitaxial stabilization on LaAlO_3 and YAlO_3 with the pulsed laser deposition method [56–59]. Considering a suitable lattice match for both BFO and BCO, we propose LaAlO_3 can be a very good candidate for the experimental realization of the BCO/BFO superlattice with tetragonal phase.

C. Electronic structures of the superlattices

Based on the optimized structures, we further calculate the band structures of the $(\text{BCO})_m/(\text{BFO})_1$ and $(\text{BCO})_1/(\text{BFO})_n$ superlattices. In this study, an approach of the reverse scissor correction procedure is employed. This is an empirical correction consisting of a shift of the conduction regions up and can be applied to both GGA and local-density approximation (LDA) underestimated band gaps, especially in the determination of band-gap offsets for interfaces between different semiconductors [48,60, 61]. The scissor correction method has been extensively employed in a number of calculations and the predicted band gaps and optical properties were found to agree well with experiments [49,62–64]. Here, we use a scissor operator of 1.48 eV, which corrects not only the band gap of BFO to 3.1 eV, but also the band gap of BCO to 2.42 eV, agreeing well with the experimental values of 3.1 eV [12,47] and 2.37 eV [28], respectively. The scissor operator of 1.48 eV is also applied to the $(\text{BCO})_m/(\text{BFO})_n$ superlattice structure.

TABLE IV. A comparison of the band gaps (eV) for BFO, BCO, and $(BCO)_m/(BFO)_1$ ($m = 1-5$) superlattices obtained from DFT, DFT with scissor correction, and DFT/meta-GGA-mBJ calculations.

	DFT	DFT with scissor correction	DFT/meta- GGA- mBJ	Exp.
BFO	1.62	3.1	2.92	3.1 ^{a,b}
BCO	0.94	2.42	2.27	2.37 ^c
$(BCO)_1/(BFO)_1$	0.48	1.96	2.03	
$(BCO)_2/(BFO)_1$	0.33	1.81	1.84	
$(BCO)_3/(BFO)_1$	0.27	1.75	1.77	
$(BCO)_4/(BFO)_1$	0.18	1.66	1.69	
$(BCO)_5/(BFO)_1$	0.21	1.69	1.71	

^aRef. [46].

^bRef. [47].

^cRef. [28].

The variation of the reverse scissor corrected band gap for $(BCO)_1/(BFO)_n$ and $(BCO)_m/(BFO)_1$ superlattices as a function of the number of BFO and BCO layers [Fig. 4(a)] and the calculated band structures (Fig. 5) are presented. It is shown that all the superlattices retain the direct band gap character, similar to that of BFO. In addition, based on the calculated results, it appears that the charge hybridization and carrier transport will mainly occur within the tetragonal plane rather than along the *c* axis, since the dispersion occurs along the G-X, X-M, and M-G directions while the bands are flat along the G-Z direction [65]. The band gap of the superlattices is observed to decrease markedly with the number of layers of BFO and/or BCO in a given stack height [Fig. 4(a)]. The band gap of the $(BCO)_1/(BFO)_n$ superlattices are lower than that of the $(BCO)_m/(BFO)_1$ superlattices for the same values of *n* and *m* (*n*, *m* > 1). The band-gap values for the superlattices are located within the range of 1.59–1.96 eV, which is unexpectedly smaller than that of the parent materials.

In order to verify if the scissor correction results for the superlattice structure are reliable, a series of DFT/meta-GGA calculations with the mBJ (modified-Becke-Johnson) functional are also carried out. The DFT/meta-GGA method with mBJ functional (DFT/meta-GGA-mBJ) has been reported to yield band gaps with an accuracy similar to a hybrid functional or the quasi-particle self-consistent GW approximation methods for various semiconductors/insulators, but is computationally less expensive [66]. We have performed DFT/meta-GGA-mBJ calculations on BFO, BCO, and $(BCO)_m/(BFO)_1$ (*m* = 1–5) superlattices and a comparison of the obtained band gap by DFT, DFT with scissor correction, and DFT/meta-GGA-mBJ calculations is listed in Table IV. For bulk BFO and BCO under the DFT/meta-GGA-mBJ scheme, the weight parameters (cmBJ values) of 1.4 and 1.3 are employed, respectively, and the obtained band gaps of 2.92 eV for bulk BFO and 2.27 eV for bulk BCO are in good agreement with the experimental values of 3.1

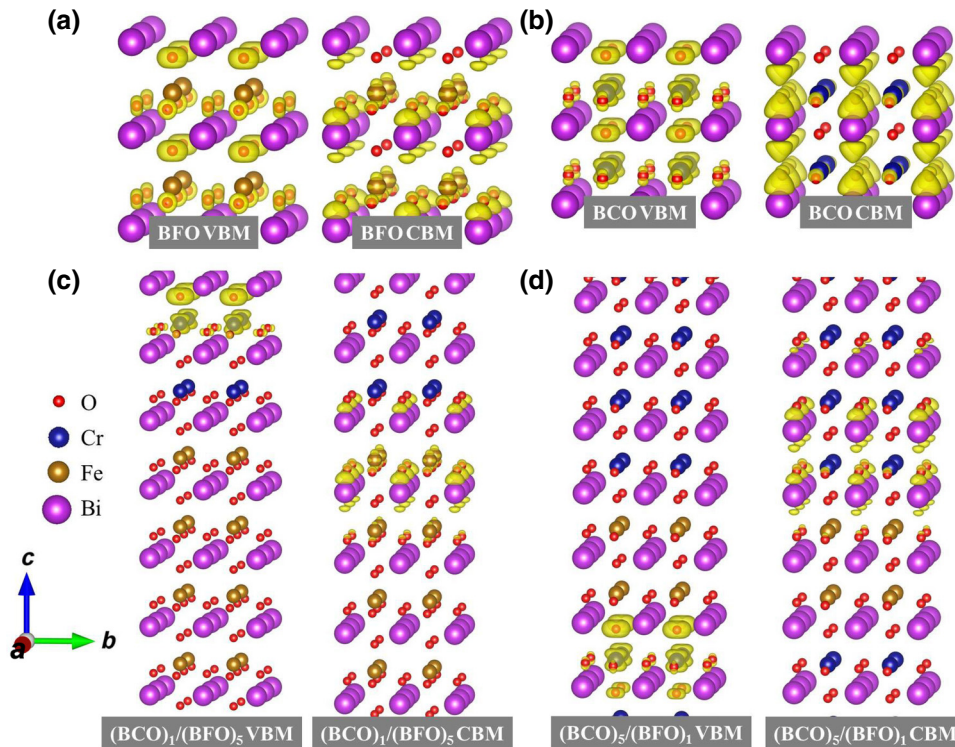


FIG. 6. Partial charge density distributions at VBM (left) and CBM (right) for (a) BFO; (b) BCO; (c) $(BCO)_1/(BFO)_5$; and (d) $(BCO)_5/(BFO)_1$.

[12,47] and 2.37 eV [28], respectively. We then apply these cmBJ values to the $(\text{BCO})_m/(\text{BFO})_1$ ($m = 1-5$) superlattices. It is noticeable that the band gap values predicted by scissor corrections compare well with those obtained from DFT/meta-GGA-mBJ and both methods predict similar band gap variation trends, confirming the reliability of the current predicted band gap values.

Furthermore, the obtained value (1.59–1.96 eV) is also substantially smaller than that of the alloyed $\text{Bi}(\text{Fe}, \text{Cr})\text{O}_3$

sample [27]. Similar results wherein the band gap of a composite compound is smaller than that of the parent materials have also been reported in superlattices of $(\text{GaN})_1/(\text{ZnO})_1$ [67] and (0001)-oriented wurtzite $(\text{GaN})_n/(\text{AlN})_n$ ($n = 10, 12, 14$) [68] as well as nanocomposites of carbon-ZrO₂ [69], NiO:TiO₂ [70], and Fe₂O₃-Cr₂O₃ systems [71–73].

For the band gap reduction with the increasing layer number of BFO or BCO, the lattice strain induced by

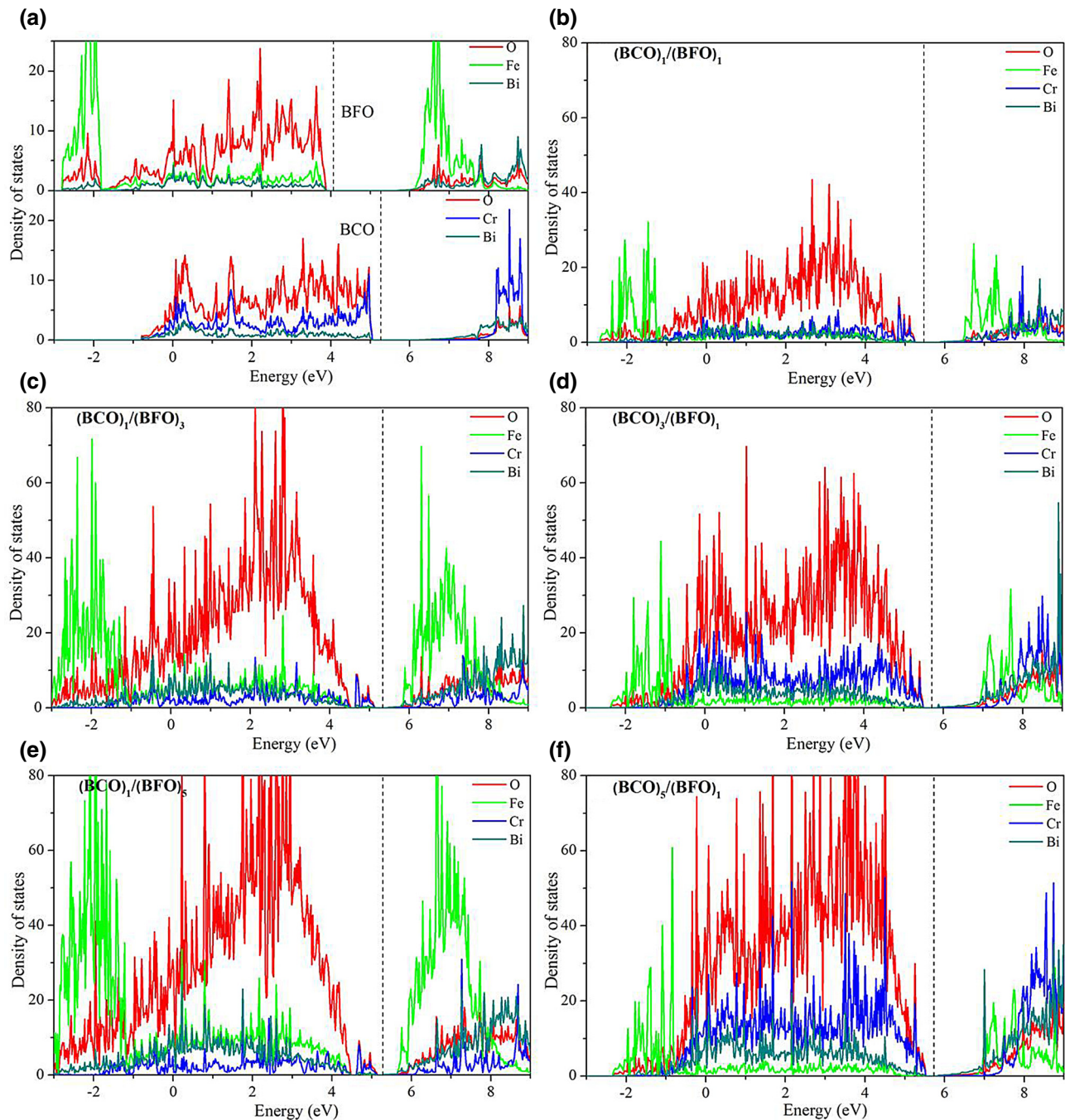


FIG. 7. Atomic projected density of state distribution for (a) parent materials (up: BFO; down: BCO); (b) $(\text{BCO})_1/(\text{BFO})_1$; (c) $(\text{BCO})_1/(\text{BFO})_3$; (d) $(\text{BCO})_3/(\text{BFO})_1$; (e) $(\text{BCO})_1/(\text{BFO})_5$ and (f) $(\text{BCO})_5/(\text{BFO})_1$. The Fermi level is indicated by the dashed line.

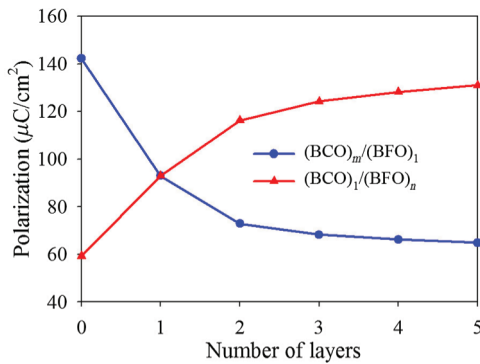


FIG. 8. Variation of polarization for $(\text{BCO})_m/(\text{BFO})_1$ and $(\text{BCO})_1/(\text{BFO})_n$ ($m, n = 0, 1, 2, 3, 4, 5$) as a function of the number of layers.

the lattice mismatch between BFO and BCO may be one of the reasons responsible. In order to explore how the lattice strain influences the band gap, we investigate the band gap of BFO and BCO within 2% tensile and compressive strains, respectively. The variation of band gap as a function of strain is illustrated [Fig. 4(b)]. It is shown that the band gaps of both BFO and BCO decrease monotonously upon decreasing the compressive strain and increasing the tensile strain level. This predicted trend is consistent with a recent experimental observation that film epitaxially grown on compressive substrates (e.g., LaAlO_3 and YAlO_3) exhibits a relatively larger optical band gap than a film grown on a tensile substrate (e.g., DyScO_3) [46,47,74,75].

For $(\text{BCO})_m/(\text{BFO})_1$ superlattices, the interlayer distances between BCO layers are comparable to that of bulk BCO and the interlayer distances between the BFO layers are much smaller than that of bulk BFO, i.e., the tensile strain of BFO dominates in the $(\text{BCO})_m/(\text{BFO})_1$ superlattices and the tensile strain increases with the increasing layer number of BCO. As for $(\text{BCO})_1/(\text{BFO})_n$ superlattices, the interlayer distances between BFO layers are comparable to that of bulk BFO and the interlayer distances between BCO layers are much larger than that of bulk BCO, i.e., the compressive strain of BCO dominates in the $(\text{BCO})_1/(\text{BFO})_n$ superlattices and the compressive strain increases with the increasing layer number of BFO.

It should be pointed out that the $(\text{BCO})_m/(\text{BFO})_n$ superlattice cannot be free-standing experimentally and a suitable substrate is necessary. Considering the error between calculated values and experimental measurements, the in-plane lattice constants of $(\text{BCO})/(\text{BFO})$ superlattices will vary from 3.738 to 3.885 Å. Therefore, the LaAlO_3 (LAO), with a lattice constant of 3.79 Å, will be a suitable substrate for the synthesis of a BFO/BCO superlattice. The lattice mismatch between the substrate and the superlattice structure is estimated to be 1.3%–2.5% and the induced lattice strain varies from –2.4% to 1.4%. We

also study the strain effect on the band gap of the superlattice. The representative results of $(\text{BCO})_1/(\text{BFO})_1$ and $(\text{BCO})_1/(\text{BFO})_5$ are also shown in Fig. 4(b). It is clearly seen that the superlattice demonstrates a similar trend of a strain-dependent band gap as a single phase of BFO and BCO. However, the band gap variation is much smaller, for example, the band gap of the $(\text{BCO})_1/(\text{BFO})_1$ superlattice changes from 2.06 to 1.94 eV corresponding to a –2% compressive strain to a 2% tensile strain. Therefore, the epitaxial strain is not expected to significantly impact the band gap values of the superlattice systems.

In order to understand the origin of the unexpected band-gap reduction, further electronic structure calculations are necessary. The partial charge density distributions at the valence-band maxima (VBM) and conduction-band minima (CBM) for BFO, BCO, and the $(\text{BCO})_1/(\text{BFO})_5$ and $(\text{BCO})_5/(\text{BFO})_1$ superlattices are illustrated (Fig. 6). It is found that holes at the VBM for BFO are mainly contributed by two types of oxygen anions, while the electrons at the CBM are mainly located on the A-site Bi and O_A atoms, respectively, and slightly on the B-site Fe atom. For the BCO, the charge density distribution is remarkably different. The holes at the VBM are mainly gathered on the

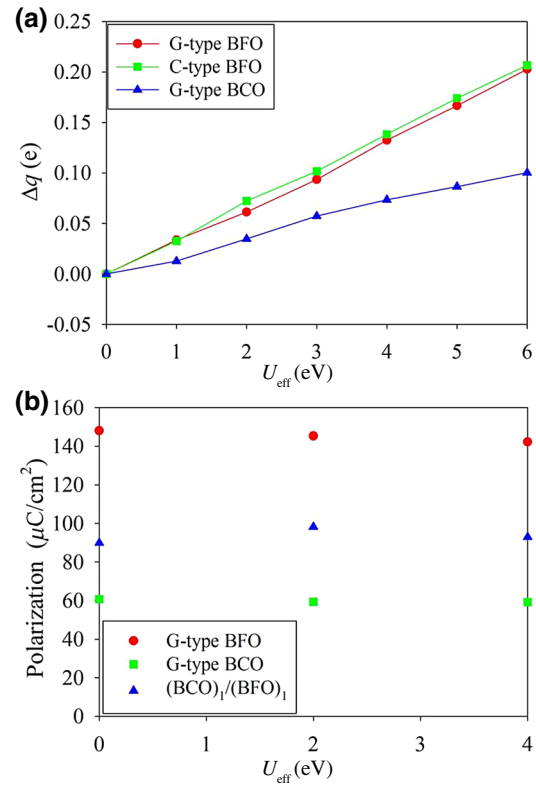


FIG. 9. (a) Variation of transition metal (TM) partial charge Δq with U_{eff} value for bulk BFO and BCO. The TMs are Fe and Cr in the BFO and BCO, respectively; (b) variation of polarization for bulk BFO, BCO, and $(\text{BCO})_1/(\text{BFO})_1$ superlattices as a function of U_{eff} value.

two types of O atoms as well as on B-site Cr atoms, while the electrons at the CBM are mainly contributed by the A-site Bi and O_A atoms. The different valence/conduction band characteristics of these two compounds originate from the different electron negativities of the transition-metal cations and thus, the different electronic structures of BFO and BCO. The valence bands of BFO are mainly contributed by O 2p orbitals, whereas the O 2p and Cr 3d states dominate the valance bands of BCO in the band edge near the Fermi level (Fig. 7) due to the slighter higher atomic energy position for Cr 3d orbitals than Fe 3d orbitals. These results indicate that electron redistribution should be expected when the BFO and BCO are simultaneously incorporated in the same superlattice structures. Comparing the charge distribution of the $(\text{BCO})_1/(\text{BFO})_5$ superlattice with that of bulk BFO and BCO, we find that the holes at the VBM for the $(\text{BCO})_1/(\text{BFO})_5$ superlattices are mainly contributed by the interfacial Cr 3d and O 2p orbitals, and the electrons at the CBM are mainly gathered on the interfacial Fe 3d, Bi 6p, and a few O_A 2p orbitals. For the $(\text{BCO})_5/(\text{BFO})_1$ superlattices, the charge distribution of the VBM and the CBM are similar to the $(\text{BCO})_1/(\text{BFO})_5$ superlattices, where the holes at the VBM are mainly contributed by the Cr and O_B ions and the electrons at the CBM are mainly gathered on the Bi and O_A ions. The atomic projected densities of state distribution for bulk BFO, bulk BCO, $(\text{BCO})_1/(\text{BFO})_n$, and $(\text{BCO})_n/(\text{BFO})_1$ ($n, m = 1, 3, 5$) superlattices are illustrated (Fig. 7). It is noted that the Fermi level of the BFO is shifted to a higher binding energy when the superlattice structure is formed, accompanied by the upward shift of the valence bands. As compared with the DOS distribution of the $(\text{BCO})_1/(\text{BFO})_1$ superlattice, it is noted that the Fermi levels shift slightly to the higher binding energy level and lower binding energy level for $(\text{BCO})_1/(\text{BFO})_n$ and $(\text{BCO})_m/(\text{BFO})_1$ superlattices, respectively. As for $(\text{BCO})_1/(\text{BFO})_n$ superlattices, the valence bands are mainly contributed by O 2p and Fe 3d states; in the case of $(\text{BCO})_m/(\text{BFO})_1$ superlattices, the O 2p and Cr 3d states dominate the valence bands. The conduction bands of $(\text{BCO})_1/(\text{BFO})_n$ and $(\text{BCO})_m/(\text{BFO})_1$ superlattices also exhibit different characters. For the $(\text{BCO})_1/(\text{BFO})_n$ superlattices, the conduction bands shift towards Fermi level. Consequently, the band gaps of the $(\text{BCO})_1/(\text{BFO})_n$ and $(\text{BCO})_m/(\text{BFO})_1$ superlattices are much lower than that of BFO.

D. Spontaneous polarization

An excellent ferroelectric PV material should have not only a low band gap and high photocurrent, but also a large spontaneous polarization. The polarization can be estimated by

$$\Delta P_\alpha \cong \sum_{j\beta} (\partial P_\alpha / \partial \mu_{j\beta})(\mu_{j\beta} - \mu_{0j\beta}) \\ = \frac{e}{\Omega} \sum_{j\beta} Z_{j\alpha\beta}^* \Delta \mu_{j\beta},$$

where $\Delta \mu_{j\beta}$ is the displacement of ions j in the Cartesian direction β , $Z_{j\alpha\beta}^*$ is the Born effective charge tensor, e is the charge of an electron, and Ω is the cell volume [41]. In this work, cubic BFO is used as the centrosymmetric reference structure, which is described by the zero subscript. The calculated polarization for the tetragonal-like BFO by this method is $142.3 \mu\text{C}/\text{cm}^2$, which agrees well with the experimental data of $150\text{--}158 \mu\text{C}/\text{cm}^2$ [13,42] and other prior calculated values of $136\text{--}145 \mu\text{C}/\text{cm}^2$ [59,76,77]. The polarization as a function of the BFO and BCO layer numbers is plotted (Fig. 8). It is shown that the polarizations of all superlattices are located in the range of $64.8\text{--}131.0 \mu\text{C}/\text{cm}^2$. The polarizations of the superlattices decrease with the increasing number of BCO layers, but increase with the increasing BFO layers, which is similar to the variation of the c/a ratio with layer numbers of both BFO and BCO. A similar dependence has been

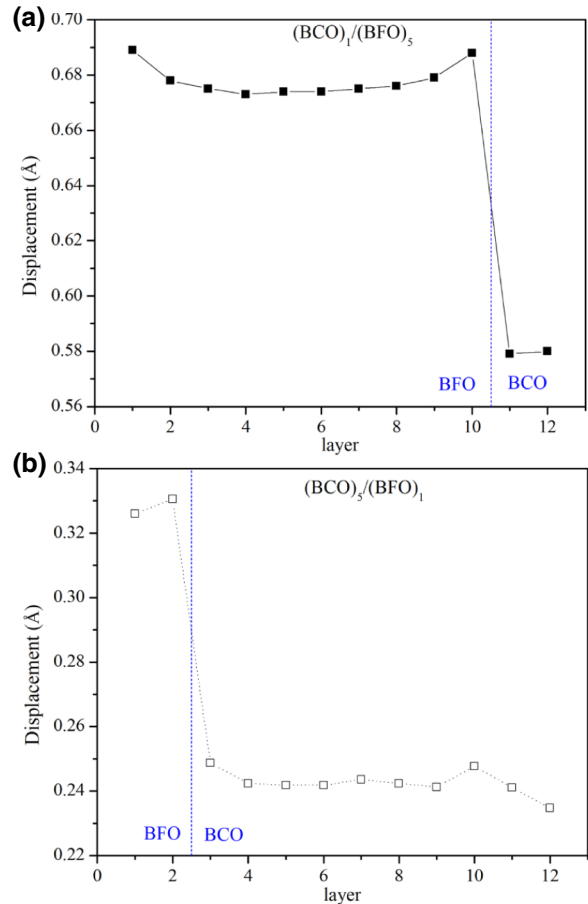


FIG. 10. Local displacement between Fe/Cr ions and O ions for (a) $(\text{BCO})_1/(\text{BFO})_5$ and (b) $(\text{BCO})_5/(\text{BFO})_1$ superlattices.

reported in tetragonal $(\text{BaZrO}_3)_m/(\text{BaTiO}_3)_n$ superlattices that have a large c/a ratio and large polarization [52]. We find that the polarizations of the superlattices are mainly contributed by the transition elements and the O^{2-} ions, and the contribution of O_A is larger than that of O_B . The direction of polarization of transition elements is in opposition to that of O and Bi atoms. In addition, the polarization of $92.9\text{--}131.0 \mu\text{C}/\text{cm}^2$ for the $(\text{BCO})_1/(\text{BFO})_n$ superlattices is larger than the polarization of $64.8\text{--}92.9 \mu\text{C}/\text{cm}^2$ for the $(\text{BCO})_m/(\text{BFO})_1$ superlattices, and the value of $131.0 \mu\text{C}/\text{cm}^2$ for the $(\text{BCO})_1/(\text{BFO})_5$ superlattices is the largest among all the investigated superlattices. This likely arises from the combined effects of lattice strain in the BFO layers due to lattice mismatch and the distorted octahedra in both the BFO and BCO.

In this study, a DFT + U method is employed to investigate the band gaps and polarizations of $(\text{BCO})_m/(\text{BFO})_n$ superlattices. In order to investigate the effects of the U_{eff} value on the polarization, the impact of the U_{eff} value on the Fe partial charge change Δq has been investigated for bulk BFO with both G- and C-type AFM states, and the results are plotted (Fig. 9(a)). It is shown that the Δq increases with the increasing U_{eff} value, i.e., the charge tends to be away from the Fe and localize on its neighboring O ions for both G- and C-type BFO. For G-type BCO, a similar trend has been observed. These results suggest that the choice of the U_{eff} value affects the exact value of the atomic charge. The variation of polarization for bulk BFO, BCO, and $(\text{BCO})_1/(\text{BFO})_1$ superlattices as a function of U_{eff} value are presented [Fig. 9(b)]. It turns out that the choice of U_{eff} value has slight influences on the polarization. This is because the polarization is mainly determined by the charge and displacement of all the ions. Although the U_{eff} value greatly affects the charges of Fe and Cr, it also greatly affects the charges of anions simultaneously, i.e., it is a synergistic effect. On the other hand, the U_{eff} value has a small impact on the displacement of all ions. Consequently, the polarization of the materials is affected slightly by the U_{eff} values.

The local polarization can also be described by the local displacement between transition-metal cations and oxygen anions in the superlattices [78]. The local displacement between the Cr/Fe and O ions for the $(\text{BCO})_1/(\text{BFO})_5$ and $(\text{BCO})_5/(\text{BFO})_1$ superlattices along the [001] direction is shown (Fig. 10). It can be seen that both the displacements of the BFO and BCO parts for the $(\text{BCO})_1/(\text{BFO})_5$ and $(\text{BCO})_5/(\text{BFO})_1$ superlattices fluctuate slightly with increasing distance from the interface, and there is a sharp decrease at the interface, indicative of a sharp change in the polarization at the $\text{BiFeO}_3/\text{BiCrO}_3$ interface. This polarization discontinuity has been observed in $\text{BiFeO}_3/\text{SrTiO}_3$ [79], $\text{LaAlO}_3/\text{PbTiO}_3$ [78], $\text{LaAlO}_3/\text{SrTiO}_3$ [80,81], $\text{LaCrO}_3/\text{SrTiO}_3$ [82], and $\text{PbTiO}_3/\text{SrTiO}_3$ [83] heterostructures, in which there is an internal electric field and a two-dimensional-like electronic gas is formed at the

interface. In this study, the polarization discontinuity at the interface and the induced charge reconstruction also contribute to the remarkable reduction in the band gap for the $(\text{BCO})_m/(\text{BFO})_n$ superlattices.

IV. CONCLUSION

In summary, this work provides a systematic DFT + U investigation of $(\text{BCO})_m/(\text{BFO})_1$ and $(\text{BCO})_1/(\text{BFO})_n$ superlattices ($m, n = 1, 2, 3, 4, 5$) to understand how the superlattice structuring and periodicity influence the geometric structure and electronic properties. Due to the lattice mismatch between BCO and BFO, significant compression of the BiFeO_3 layer and large relaxation of the BCO layers along the [001] direction are found for the $(\text{BCO})_m/(\text{BFO})_1$ superlattices, and considerable expansion of the BCO layer and a remarkable relaxation of the BFO layers are found for the $(\text{BCO})_1/(\text{BFO})_n$ superlattices. Meanwhile, the octahedral distortion in the $(\text{BCO})_1/(\text{BFO})_n$ superlattices is found to be more significant than that in the $(\text{BCO})_m/(\text{BFO})_1$ superlattices. For all the considered superlattices, the band gap decreases significantly with increasing number of layers of BFO and/or BCO, and the band gap of the $(\text{BCO})_1/(\text{BFO})_n$ superlattices is lower than that of the $(\text{BCO})_m/(\text{BFO})_1$ superlattices for any given value of n and m ($n, m > 1$). Additionally, all the superlattices retain the direct character of the BFO. Surprisingly, the $(\text{BCO})_m/(\text{BFO})_n$ superlattices show significant band-gap reduction by as much as 1.5 eV. The optimized band gap of 1.6 eV is not only smaller than that of both BFO and BCO, but also smaller than the alloyed $\text{BiFe}_x\text{Cr}_y\text{O}_3$ samples, thus implying good potential for visible-light absorption. The polarization is found to be $92.9\text{--}131.0 \mu\text{C}/\text{cm}^2$ for the $(\text{BCO})_1/(\text{BFO})_n$ superlattices and $64.8\text{--}92.9 \mu\text{C}/\text{cm}^2$ for the $(\text{BCO})_m/(\text{BFO})_1$ superlattices, among which the value of $131 \mu\text{C}/\text{cm}^2$ for the $(\text{BCO})_1/(\text{BFO})_5$ superlattice is the largest and is comparable to the polarization of BFO. These results demonstrate that superlattice ordering can be a new strategy to design low-band-gap semiconductors with fundamental band gaps much smaller than those of the parent materials, thus opening new perspectives for ferroelectric photovoltaics.

ACKNOWLEDGMENTS

H.Y.X. was supported by the NSAF Joint Foundation of China (Grant No. U1530129). Z.J. Liu was supported by National Natural Science Foundation of China (Grant No. 11464025), the New Century Excellent Talents in University under Grant No. NCET-11-0906 and the Key Talent Foundation of Gansu Province. L.Q. was supported by National Natural Science Foundation of China (Grant No. 1174044) and the Young 1000-talent Program. D.J.S. was supported by the Department of Energy through the S3TEC Energy Frontier Research Center, award No.

.DE-SC0001299. L.W.M. acknowledges the support of the National Science Foundation under Grant No. DMR-1608938. The theoretical calculations were performed using the supercomputer resources at TianHe-1 located at National Supercomputer Center in Tianjin.

-
- [1] P. Lopez-Varo, L. Bertoluzzi, J. Bisquert, M. Alexe, M. Coll, J. Huang, J. Antonio Jimenez-Tejada, T. Kirchartz, R. Nechache, F. Rosei, and Y. Yuan, Physical aspects of ferroelectric semiconductors for photovoltaic solar energy conversion, *Phys. Rep.* **653**, 1 (2016).
- [2] S. Y. Yang, L. W. Martin, S. J. Byrnes, T. E. Conry, S. R. Basu, D. Paran, L. Reichertz, J. Ihlefeld, C. Adamo, A. Melville, Y.-H. Chu, C.-H. Yang, J. L. Musfeldt, D. G. Schlom, J. W. Ager III, and R. Ramesh, Photovoltaic effects in BiFeO_3 , *Appl. Phys. Lett.* **95**, 062909 (2009).
- [3] B. Chen, J. Shi, X. Zheng, Y. Zhou, K. Zhu, and S. Priya, Ferroelectric solar cells based on inorganic-organic hybrid perovskites, *J. Mater. Chem. A* **3**, 7699 (2015).
- [4] Y. Liu, S. Wang, Z. Chen, and L. Xiao, Applications of ferroelectrics in photovoltaic devices, *Sci. China Mater.* **59**, 851 (2016).
- [5] C. Paillard, X. Bai, I. C. Infante, M. Guennou, G. Geneste, M. Alexe, J. Kreisel, and B. Dkhil, Photovoltaics with ferroelectrics: Current status and beyond, *Adv. Mater.* **28**, 5153 (2016).
- [6] Y. Yuan, Z. Xiao, B. Yang, and J. Huang, Arising applications of ferroelectric materials in photovoltaic devices, *J. Mater. Chem. A* **2**, 6027 (2014).
- [7] S. Y. Yang, J. Seidel, S. J. Byrnes, P. Shafer, C.-H. Yang, M. D. Rossell, P. Yu, Y.-H. Chu, J. F. Scott, J. W. Ager, L. W. Martin, and R. Ramesh, Above-bandgap voltages from ferroelectric photovoltaic devices, *Nat. Nanotechnol.* **5**, 143 (2010).
- [8] V. M. Fridkin, Bulk photovoltaic effect in noncentrosymmetric crystals, *Crystallogr. Rep.* **46**, 654 (2001).
- [9] L. Pintilie, I. Vrejoiu, G. L. Rhun, and M. Alexe, Short-circuit photocurrent in epitaxial lead zirconate-titanate thin films, *J. Appl. Phys.* **101**, 064109 (2007).
- [10] J. Chakrabarty, R. Nechache, S. Li, M. Nicklaus, A. Ruediger, F. Rosei, and D. D. Viehland, Photovoltaic properties of multiferroic $\text{BiFeO}_3/\text{BiCrO}_3$ heterostructures, *J. Am. Ceram. Soc.* **97**, 1837 (2014).
- [11] Y. Li and D. J. Singh, Properties of the ferroelectric visible light absorbing semiconductors: $\text{Sn}_2\text{P}_2\text{S}_6$ and $\text{Sn}_2\text{P}_2\text{Se}_6$, *Phys. Rev. Mater.* **1**, 075402, (2017).
- [12] P. Chen, N. J. Podraza, X. S. Xu, A. Melville, E. Vlahos, V. Gopalan, R. Ramesh, D. G. Schlom, and J. L. Musfeldt, Optical properties of quasi-tetragonal BiFeO_3 thin films, *Appl. Phys. Lett.* **96**, 131907 (2010).
- [13] K. Y. Yun, D. Ricinschi, T. Kanashima, M. Noda, and M. Okuyama, Giant ferroelectric polarization beyond $150 \mu\text{C}/\text{cm}^2$ in BiFeO_3 thin film, *Jpn. J. Appl. Phys.* **43**, L647 (2004).
- [14] Y.-H. Chu, L. W. Martin, M. B. Holcomb, and R. Ramesh, Controlling magnetism with multiferroics, *Mater. Today* **10**, 16 (2007).
- [15] C. Ederer and N. A. Spaldin, Effect of Epitaxial Strain on the Spontaneous Polarization of Thin Film Ferroelectrics, *Phys. Rev. Lett.* **95**, 257601 (2005).
- [16] S. Gupta, M. Tomar, and V. Gupta, Ferroelectric photovoltaic response to structural transformations in doped BiFeO_3 derivative thin films, *Mater. Des.* **105**, 296 (2016).
- [17] Y. Sun, X. Liu, J. Zeng, J. Yan, D. Shi, and H. Liu, Photovoltaic effects in polarized polycrystalline BiFeO_3 films, *J. Electron. Mater.* **44**, 4207 (2015).
- [18] S. M. Young, F. Zheng, and A. M. Rappe, First-Principles Calculation of the Bulk Photovoltaic Effect in Bismuth Ferrite, *Phys. Rev. Lett.* **109**, 236601 (2012).
- [19] P. P. Biswas, T. Chinthakuntla, D. Duraisamy, G. N. Venkatesan, S. Venkatachalam, and P. Murugavel, Photovoltaic and photo-capacitance effects in ferroelectric BiFeO_3 thin film, *Appl. Phys. Lett.* **110**, 192906 (2017).
- [20] M. M. Yang, Z. D. Luo, D. J. Kim, and M. Alexe, Bulk photovoltaic effect in monodomain BiFeO_3 thin films, *Appl. Phys. Lett.* **110**, 183902 (2017).
- [21] R. Nechache, C. Harnagea, S. Li, L. Cardenas, W. Huang, J. Chakrabarty, and F. Rosei, Bandgap tuning of multiferroic oxide solar cells, *Nat. Photonics* **9**, 61 (2015).
- [22] R. Nechache, P. Gupta, C. Harnagea, and A. Pignolet, Enhanced magnetism in epitaxial $\text{BiFeO}_3/\text{BiCrO}_3$ multiferroic heterostructures, *Appl. Phys. Lett.* **91**, 222908 (2007).
- [23] S. K. Singh, S. Shanthi, and H. Ishiwara, Reduced leakage current in $\text{BiFeO}_3\text{-BiCrO}_3$ nanocomposite films formed by chemical solution deposition, *J. Appl. Phys.* **108**, 054102 (2010).
- [24] S. Gepraegs, M. Opel, S. T. B. Goennenwein, and R. Gross, Multiferroic materials based on artificial thin film heterostructures, *Philos. Mag. Lett.* **87**, 141 (2007).
- [25] P. Couture, G. V. M. Williams, J. Kennedy, J. Levener, P. P. Murmu, S. V. Chong, and S. Rubanov, Multiferroic nanocrystalline BiFeO_3 and BiCrO_3 thin films prepared by ion beam sputtering, *Int. J. Nanotechnol.* **14**, 56 (2017).
- [26] J. W. Kim, C. M. Raghavan, J. W. Kim, and S. S. Kim, Multiferroic properties of a $\text{BiCrO}_3/\text{BiFeO}_3$ double-layered thin film prepared by chemical solution deposition, *Ceram. Int.* **41**, 7211 (2015).
- [27] L. Qiao, S. Zhang, H. Y. Xiao, D. J. Singh, K. H. L. Zhang, Z. J. Liu, X. T. Zu, and S. Li, Orbital controlled band gap engineering of tetragonal BiFeO_3 for optoelectronic applications, *J. Mater. Chem. C* **6**, 1239 (2018).
- [28] C. Nie, S. Zhao, Y. Bai, and Q. Lu, The ferroelectric photovoltaic effect of $\text{BiCrO}_3/\text{BiFeO}_3$ bilayer composite films, *Ceram. Int.* **42**, 14036 (2016).
- [29] S. Chakraverty, K. Yoshimatsu, Y. Kozuka, H. Kumigashira, M. Oshima, T. Makino, A. Ohtomo, and M. Kawasaki, Magnetic and electronic properties of ordered double-perovskite La_2VMnO_6 thin films, *Phys. Rev. B* **84**, 132411 (2011).
- [30] S. Chakraverty, A. Ohtomo, D. Okuyama, M. Saito, M. Okude, R. Kumai, T. Arima, Y. Tokura, S. Tsukimoto, Y. Ikuhara, and M. Kawasaki, Ferrimagnetism and spontaneous ordering of transition metals in double perovskite $\text{La}_2\text{CrFeO}_6$ films, *Phys. Rev. B* **84**, 064436 (2011).

- [31] M. P. Singh, K. D. Truong, S. Jandl, and P. Fournier, Long-range Ni/Mn structural order in epitaxial double perovskite $\text{La}_2\text{NiMnO}_6$ thin films, *Phys. Rev. B* **79**, 224421 (2009).
- [32] K. Ueda, H. Tabata, and T. Kawai, Ferromagnetism in LaFeO_3 - LaCrO_3 superlattices, *Science* **280**, 1064 (1998).
- [33] L. Qiao, H. Y. Xiao, S. M. Heald, M. E. Bowden, T. Varga, G. J. Exarhos, M. D. Biegalski, I. N. Ivanov, W. J. Weber, T. C. Droubay, and S. A. Chambers, The impact of crystal symmetry on the electronic structure and functional properties of complex lanthanum chromium oxides, *J. Mater. Chem. C* **1**, 4527 (2013).
- [34] L. Qiao, K. H. L. Zhang, M. E. Bowden, T. Varga, V. Shuttanandan, R. Colby, Y. Du, B. Kabius, P. V. Sushko, M. D. Biegalski, and S. A. Chambers, The impacts of cation stoichiometry and substrate surface quality on nucleation, structure, defect formation, and intermixing in complex oxide heteroepitaxy- LaCrO_3 on SrTiO_3 (001), *Adv. Funct. Mater.* **23**, 2953 (2013).
- [35] N. Ichikawa, M. Arai, Y. Imai, K. Hagiwara, H. Sakama, M. Azuma, Y. Shimakawa, M. Takano, Y. Kotaka, M. Yonetani, H. Fujisawa, M. Shimizu, K. Ishikawa, and Y. Cho, Multiferroism at room temperature in BiFeO_3 / BiCrO_3 (111) artificial superlattices, *Appl. Phys. Express* **1**, 101302 (2008).
- [36] G. Kresse and J. Hafner, Ab initio molecular-dynamics for liquid-metals, *Phys. Rev. B* **47**, 558 (1993).
- [37] G. Kresse and J. Furthmüller, Efficiency of ab-initio total energy calculations for metals and semiconductors using a plane-wave basis set, *Comp. Mater. Sci.* **6**, 15 (1996).
- [38] J. P. Perdew, K. Burke, and M. Ernzerhof, Generalized Gradient Approximation Made Simple, *Phys. Rev. Lett.* **77**, 3865 (1996).
- [39] V. I. Anisimov, F. Aryasetiawan, and A. I. Lichtenstein, First-principles calculations of the electronic structure and spectra of strongly correlated systems: The LDA + U method, *J. Phys.-Condens. Matter* **9**, 767 (1997).
- [40] H. Dong, C. Chen, S. Wang, W. Duan, and J. Li, Elastic properties of tetragonal BiFeO_3 from first-principles calculations, *Appl. Phys. Lett.* **102**, 182905 (2013).
- [41] J. B. Neaton, C. Ederer, U. V. Waghmare, N. A. Spaldin, and K. M. Rabe, First-principles study of spontaneous polarization in multiferroic BiFeO_3 , *Phys. Rev. B* **71**, 014113 (2005).
- [42] D. Ricinschi, K. Y. Yun, and M. Okuyama, A mechanism for the $150 \mu\text{C}/\text{cm}^2$ polarization of BiFeO_3 films based on first-principles calculations and new structural data, *J. Phys.-Condens. Matter* **18**, L97 (2006).
- [43] O. Dieguez, O. E. Gonzalez-Vazquez, J. C. Wojdel, and J. Iniguez, First-principles predictions of low-energy phases of multiferroic BiFeO_3 , *Phys. Rev. B* **83**, 094105 (2011).
- [44] N. Feng, W. Mi, X. Wang, Y. Cheng, and U. Schwingenschlögl, Superior properties of energetically stable $\text{La}_{2/3}\text{Sr}_{1/3}\text{MnO}_3$ /tetragonal BiFeO_3 multiferroic superlattices, *ACS Appl. Mater. Interfaces* **7**, 10612 (2015).
- [45] T. P. Comyn, T. Stevenson, M. Al-Jawad, S. L. Turner, R. I. Smith, A. J. Bell, and R. Cywinski, High temperature neutron diffraction studies of 0.9BiFeO_3 - 0.1PbTiO_3 , *J. Appl. Phys.* **105**, 094108 (2009).
- [46] H. L. Liu, M. K. Lin, Y. R. Cai, C. K. Tung, and Y. H. Chu, Strain modulated optical properties in BiFeO_3 thin films, *Appl. Phys. Lett.* **103**, 181907 (2013).
- [47] C. Himcinschi, A. Bhatnagar, A. Talkenberger, M. Barchuk, D. R. T. Zahn, D. Rafaja, J. Kortus, and M. Alexe, Optical properties of epitaxial BiFeO_3 thin films grown on LaAlO_3 , *Appl. Phys. Lett.* **106**, 012908 (2015).
- [48] S. Mamoun, A. E. Merad, and L. Guilbert, Energy band gap and optical properties of lithium niobate from ab initio calculations, *Comp. Mater. Sci.* **79**, 125 (2013).
- [49] S. Froyen, D. M. Wood, and A. Zunger, Structural and electronic properties of epitaxial thin-layer Si_nGe_n superlattices, *Phys. Rev. B* **37**, 6893 (1988).
- [50] D. H. Kim, H. N. Lee, M. Varela, and H. M. Christen, Antiferroelectricity in multiferroic BiCrO_3 epitaxial films, *Appl. Phys. Lett.* **89**, 162904 (2006).
- [51] T. Qi, I. Grinberg, and A. M. Rappe, Correlations between tetragonality, polarization, and ionic displacement in PbTiO_3 -derived ferroelectric perovskite solid solutions, *Phys. Rev. B* **82**, 134113 (2010).
- [52] M. P. K. Sahoo, Y. Zhang, and J. Wang, Enhancement of ferroelectric polarization in layered BaZrO_3 / BaTiO_3 superlattices, *Phys. Lett. A* **380**, 299 (2016).
- [53] C. Zuo, S. Lu, X. Zhou, and Y. Zhang, Dependence of the structures and properties on LaAlO_3 cap layer in LaAlO_3 / BaTiO_3 superlattices, *Appl. Phys. Lett.* **92**, 012913 (2008).
- [54] T. Choi and J. Lee, Structural and dielectric properties of artificial PbZrO_3 / PbTiO_3 superlattices grown by pulsed laser deposition, *Thin Solid Films* **475**, 283 (2005).
- [55] H. M. Christen, E. D. Specht, S. S. Silliman, and K. S. Harshavardhan, Ferroelectric and antiferroelectric coupling in superlattices of paraelectric perovskites at room temperature, *Phys. Rev. B* **68**, 020101 (2003).
- [56] R. J. Zeches, M. D. Rossell, J. X. Zhang, A. J. Hatt, Q. He, C. H. Yang, A. Kumar, C. H. Wang, A. Melville, C. Adamo, G. Sheng, Y. H. Chu, J. F. Ihlefeld, R. Erni, C. Ederer, V. Gopalan, L. Q. Chen, D. G. Schlom, N. A. Spaldin, L. W. Martin, and R. Ramesh, A strain-driven morphotropic phase boundary in BiFeO_3 , *Science* **326**, 977 (2009).
- [57] M. D. Rossell, R. Erni, M. P. Prange, J. C. Idrobo, W. Luo, R. J. Zeches, S. T. Pantelides, and R. Ramesh, Atomic Structure of Highly Strained BiFeO_3 Thin Films, *Phys. Rev. Lett.* **108**, 047601 (2012).
- [58] H. Bea, B. Dupe, S. Fusil, R. Mattana, E. Jacquet, B. Warot-Fonrose, F. Wilhelm, A. Rogalev, S. Petit, V. Cros, A. Anane, F. Petroff, K. Bouzehouane, G. Geneste, B. Dkhil, S. Lisenkov, I. Ponomareva, L. Bellaiche, M. Bibes, and A. Barthélémy, Evidence for Room-Temperature Multiferroicity in a Compound with a Giant Axial Ratio, *Phys. Rev. Lett.* **102**, 217603 (2009).
- [59] J. X. Zhang, Q. He, M. Trassin, W. Luo, D. Yi, M. D. Rossell, P. Yu, L. You, C. H. Wang, C. Y. Kuo, J. T. Heron, Z. Hu, R. J. Zeches, H. J. Lin, A. Tanaka, C. T. Chen, L. H. Tjeng, Y. H. Chu, and R. Ramesh, Microscopic Origin of the Giant Ferroelectric Polarization in Tetragonal-Like BiFeO_3 , *Phys. Rev. Lett.* **107**, 147602 (2011).
- [60] M. Lannoo and M. Schlüter, Calculation of the Kohn-Sham potential and its discontinuity for a model-semiconductor, *Phys. Rev. B* **32**, 3890 (1985).

- [61] L. Makinistian and E. A. Albanesi, Ab initio calculations of the electronic and optical properties of germanium selenide, *J. Phys.-Condens. Matter* **19**, 186211 (2007).
- [62] M. G. Brik, First-principles study of the electronic and optical properties of CuXS₂ (X = Al, Ga, In) and AgGaS₂ ternary compounds, *J. Phys.-Condens. Matter* **21**, 485502 (2009).
- [63] A. O'Hara, T. N. Nunley, A. B. Posadas, S. Zollner, and A. A. Demkov, Electronic and optical properties of NbO₂, *J. Appl. Phys.* **116**, 213705 (2014).
- [64] A. Hussain Reshak, S. Auluck, and I. V. Kityk, Specific features in the band structure and linear and nonlinear optical susceptibilities of La₂CaB₁₀O₁₉ crystals, *Phys. Rev. B* **75**, 245120 (2007).
- [65] H. J. Feng, K. Yang, W. Deng, M. M. Li, M. Z. Wang, B. Duan, F. Liu, J. S. Tian, and X. H. Guo, The origin of enhanced optical absorption of the BiFeO₃/ZnO heterojunction in the visible and terahertz regions, *Phys. Chem. Chem. Phys.* **17**, 26930 (2015).
- [66] F. Tran and P. Blaha, Accurate Band Gaps of Semiconductors and Insulators with a Semilocal Exchange-Correlation Potential, *Phys. Rev. Lett.* **102**, 226401 (2009).
- [67] M. R. Boufatah and A. E. Merad, Structural stability, elastic and electronic properties of zincblende (GaN)₁/(ZnO)₁ superlattice: Modified Becke-Johnson exchange potential, *Mater. Sci. Semicon. Proc.* **19**, 179 (2014).
- [68] X. Y. Cui, B. Delley, and C. Stampfl, Band gap engineering of wurtzite and zinc-blende GaN/AlN superlattices from first principles, *J. Appl. Phys.* **108**, 103701 (2010).
- [69] E. Bailon-Garcia, A. Elmouwahidi, F. Carrasco-Marin, A. F. Perez-Cadenas, and F. J. Maldonado-Hodar, Development of Carbon-ZrO₂ composites with high performance as visible-light photocatalysts, *Appl. Catal. B-Environ.* **217**, 540 (2017).
- [70] S. A. Rawool, M. R. Pai, A. M. Banerjee, A. Arya, R. S. Ningthoujam, R. Tewari, R. Rao, B. Chalke, P. Ayyub, A. K. Tripathi, and S. R. Bharadwaj, *p-n* Heterojunctions in NiO:TiO₂ composites with type-II band alignment assisting sunlight driven photocatalytic H₂ generation, *Appl. Catal. B-Environ.* **221**, 443 (2018).
- [71] Y. Wang, K. Lopata, S. A. Chambers, N. Govind, and P. V. Sushko, Optical absorption and band gap reduction in (Fe_{1-x}Cr_x)₂O₃ solid solutions: A first-principles study, *J. Phys. Chem. C* **117**, 25504 (2013).
- [72] H. Mashiko, T. Oshima, and A. Ohtomo, Band-gap narrowing in alpha-(Cr_xFe_{1-x})₂O₃ solid-solution films, *Appl. Phys. Lett.* **99**, 241904 (2011).
- [73] S. E. Chamberlin, Y. Wang, K. Lopata, T. C. Kaspar, A. W. Cohn, D. R. Gamelin, N. Govind, P. V. Sushko, and S. A. Chambers, Optical absorption and spectral photoconductivity in alpha-(Fe_{1-x}Cr_x)₂O₃ solid-solution thin films, *J. Phys.-Condens. Matter* **25**, 392002 (2013).
- [74] C. Himeinschi, I. Vrejoiu, M. Friedrich, E. Nikulina, L. Ding, C. Cobet, N. Esser, M. Alexe, D. Rafaja, and D. R. T. Zahn, Substrate influence on the optical and structural properties of pulsed laser deposited BiFeO₃ epitaxial films, *J. Appl. Phys.* **107**, 123524 (2010).
- [75] D. Sando, C. Carretero, M. N. Grisolia, A. Barthelemy, V. Nagarajan, and M. Bibes, Revisiting the optical band gap in epitaxial BiFeO₃ thin films, *Adv. Opt. Mater.* **6**, 1700836 (2018).
- [76] H. Matsuo, Y. Kitanaka, R. Inoue, Y. Noguchi, and M. Miyayama, Heavy Mn-doping effect on spontaneous polarization in ferroelectric BiFeO₃ thin films, *Jpn. J. Appl. Phys.* **54**, 10NA03 (2015).
- [77] D. Ricinschi, K. Y. Yun, and M. Okuyama, First-principles study of BiFeO₃ films with giant polarization and its dependence on structural parameters, *Ferroelectrics* **335**, 181 (2006).
- [78] P. X. Zhou, S. Dong, H. M. Liu, C. Y. Ma, Z. B. Yan, C. G. Zhong, and J. M. Liu, Ferroelectricity driven magnetism at domain walls in LaAlO₃/PbTiO₃ superlattices, *Sci. Rep.* **5**, 13052 (2015).
- [79] Z. Zhang, P. Wu, L. Chen, and J. Wang, First-principles prediction of a two dimensional electron gas at the BiFeO₃/SrTiO₃ interface, *Appl. Phys. Lett.* **99**, 062902 (2011).
- [80] L. Qiao, T. C. Droubay, T. Varga, M. E. Bowden, V. Shutthanandan, Z. Zhu, T. C. Kaspar, and S. A. Chambers, Epitaxial growth, structure, and intermixing at the LaAlO₃/SrTiO₃ interface as the film stoichiometry is varied, *Phys. Rev. B* **83**, 085408 (2011).
- [81] L. Qiao, T. C. Droubay, V. Shutthanandan, Z. Zhu, P. V. Sushko, and S. A. Chambers, Thermodynamic instability at the stoichiometric LaAlO₃/SrTiO₃(001) interface, *J. Phys.-Condens. Mat.* **22**, 312201 (2010).
- [82] S. A. Chambers, L. Qiao, T. C. Droubay, T. C. Kaspar, B. W. Arey, and P. V. Sushko, Band Alignment, Built-In Potential, and the Absence of Conductivity at the LaCrO₃/SrTiO₃(001) Heterojunction, *Phys. Rev. Lett.* **107**, 206802 (2011).
- [83] L. Y. Wei, C. Lian, and S. Meng, Prediction of two-dimensional electron gas mediated magnetoelectric coupling at ferroelectric PbTiO₃/SrTiO₃ heterostructures, *Phys. Rev. B* **95**, 184102 (2017).